Journal of Hazardous Materials 263P (2013) 11–19

Contents lists available at ScienceDirect

Journal of Hazardous Materials

journal homepage: www.elsevier.com/locate/jhazmat

On the role of Fe^{3+} ions in Fe_xO_y/C catalysts for hydrogen production from the photodehydrogenation of ethanol

Félix Galindo-Hernández [a,b,c,*], Jin-An Wang [c], Lifang Chen [c], Xim Bokhimi [a], Ricardo Gómez [d], Alejandro Pérez-Larios [d], Noel Nava Entzana [b]

[a] Universidad Nacional Autónoma de México (U.N.A.M.), A.P. 20-364, México City, D.F. 01000, Mexico
[b] Instituto Mexicano del Petróleo (I.M.P.), Eje Central Lázaro Cárdenas Norte 152 Col. San Bartolo Atepehuacan, México City, D.F. 07730, Mexico
[c] ESIQIE, Instituto Politécnico Nacional, Col. Zacatenco, Av. Politécnico s/n, México City, D.F. 07738, Mexico
[d] Department of Chemistry, Universidad Autónoma Metropolitana-Iztapalapa, San Rafael Atlixco 186, A.P. 55-534, México City, D.F. 09340, Mexico

HIGHLIGHTS

- Iron oxides supported on carbon are photoactive catalysts.
- Photoactivity in dehydrogenation of ethanol depends of the amount of Fe^{3+} ions present in the catalysts.
- The capacity of UV–vis absorbance by the Fe_xO_y/C catalysts is significantly dependent of the amount of Fe^{3+} ions.
- A maximum of rate constant, $K = 2125\ \mu mol\ h^{-1}$, was obtained from the sample with 30 wt% Fe.

GRAPHICAL ABSTRACT

In Fe_xO_y/C photocatalyts important effect of Fe^{3+} ions in the photodehydrogenation of the ethano was noticed.

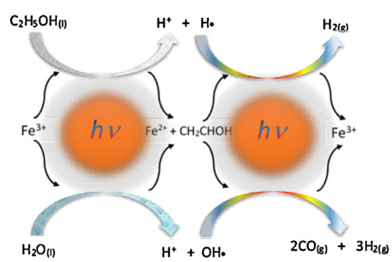

ARTICLE INFO

Article history:
Received 4 January 2013
Received in revised form 25 July 2013
Accepted 2 August 2013
Available online 12 August 2013

Keywords:
Fe_xO_y/C catalysts
Hydrogen production
Rietveld analysis
Non-local density functional theory
Ethanol photodehydrogenation

ABSTRACT

Fe_xO_y/C photocatalysts at different iron content were prepared by the incipient wet impregnation method and calcined at 773 K. The photocatalysts were characterized by means of nitrogen adsorption–desorption isotherms, surface fractal dimension, non-local density functional theory, X-ray diffraction, Rietveld refinement and UV–vis spectroscopy. The photocatalytic activity was evaluated using the photodehydrogenation of ethanol as a model reaction for the production of hydrogen. The specific surface areas of Fe_xO_y/C substrates, with 15, 20 and 30 wt% iron content, diminished from 638 to 490 m^2/g, as the iron content increased. X-ray diffraction analysis showed that iron oxides coexist as wustite and magnetite in samples with Fe contents of 15 and 20 wt%; for sample with 30 wt% Fe, wustite, magnetite and hematite phases were observed. The photophysical, textural and structural properties were modified by the hematite phase formed by thermal treatment. The Rietveld refinements denoted changes in occupancy of Fe^{3+} and Fe^{2+} in Fe_xO_y crystallites. A relationship between the Fe^{3+} ions content and the reactivity for the hydrogen production from the photodehydrogenation of ethanol (from 1360 to 2125 $\mu mol\ h^{-1}$), was evidenced.

1. Introduction

The notably increase in environmental pollution has been one of the main motivating many researchers to propose hydrogen as a promising clean fuel [1–3]. For this purpose, hydrogen production was intensively studied when produced by different sources such as water, methane, methanol and ethanol, among others, using

* Corresponding author at: Canal de San Juan Esq. Sur 24 S/N, Agrícola Oriental, Del. Iztacalco, México City, D.F. 08500, Mexico.
Tel.: +52 55 5773 6317; fax: +52 55 5773 6317.
E-mail address: felixgalindo@gmail.com (F. Galindo-Hernández).

0304-3894/$ – see front matter © 2013 Elsevier B.V. All rights reserved.
http://dx.doi.org/10.1016/j.jhazmat.2013.08.015

semiconductor materials as photocatalysts [4–8]. The photocatalytic processes in liquid phase for hydrogen production have been well accepted since they can be performed at room temperature and at a low cost in comparison with other processes. Today, some research is being focused on the use of transition metals, or metal oxides, such as Ni–Cu–Fe/Al_2O_3 [9], n-Fe_2O_3 [10] and Fe-TiO_2 [11] as photocatalysts in the production of hydrogen.

Surface formation of excited states is a consequence of optical properties characteristic of iron oxides when they are illuminated by a light source with appropriate wavelength. Those states subsequently react with the reagents. In this process, the pairs of electron–hole (e^-/h^+) are generated within the conduction and valence bands of the solid material [12]. It is reported that in photoreactions carried out in aqueous solutions, the photoelectrons generated in the bulk of Fe_2O_3 colloids may migrate toward the interface of the crystallites, so reducing generation of relatively large quantum yield of water within the solids [13]. In addition, iron-based catalysts are particularly attractive due to their low cost and abundance in the earth's crust, in comparison with other transition metals.

In the photodehydrogenation of ethanol for hydrogen production, under catalytic conditions, two hydrogen atoms are eliminated from each molecule of ethanol to form molecular hydrogen according to the following reactions [14]:

$$C_2H_5OH_{(l)} \rightarrow CH_2CHOH_{(l)} + H_{2(g)} \quad (1)$$

$$CH_2CHOH_{(l)} + H_2O_{(l)} \rightarrow 2CO_{(g)} + 3H_{2(g)} \quad (2)$$

Finally

$$C_2H_5OH_{(l)} + H_2O_{(l)} \rightarrow 2CO_{(g)} + 4H_{2(g)},\ \Delta G^\circ = 191.08\,\text{kJ mol}^{-1};\ \Delta E = 1.98\,\text{eV}$$

Although the overall reaction steps of the above reaction have been determined, details of the reaction mechanism vary according to reaction conditions and the specific catalysts employed. When iron oxides are used as photocatalysts, crystallite size effects and, particularly, Fe^{3+} concentration and lattice defects in crystalline structure of the catalysts into photodehydrogenation reaction of ethanol, are not clear.

In this research work, several Fe_xO_y/C catalysts containing FeO (wustite), FeO·Fe_2O_3 (magnetite) and Fe_2O_3 (hematite) catalysts with 15, 20 and 30 wt% Fe content were prepared by the incipient wet impregnation method. Although catalytic properties of activated carbon have already been evidenced in oxidative dehydrogenation reactions, they have been performed at 623 K [15]. Under those reaction conditions, the catalytic properties of activated carbon support can be observed. However, in this research work the photodehydrogenation of ethanol is performed under mild conditions, pH ≈ 7 and 298 K, hence, the carbon support will not be able to act as catalyst in Fe_xO_y/C materials. So that iron oxides immobilized on activated carbon, are responsible of the photodehydrogenation of ethanol. But, the textural properties of carbon such as surface area, volume pore and pore size, allow us to improve reaction kinetics.

Phase compositions, crystalline structures and lattice defects of Fe_xO_y/C catalysts were studied by X-ray diffraction, Rietveld refinement, non-local density functional theory (NLDFT) and UV–vis spectroscopic techniques. The correlation between crystalline structures and their photocatalytic properties in hydrogen production was investigated. A novel reaction mechanism in the photodehydrogenation of ethanol is proposed.

Table 1
Atomic fractional coordinates and occupancies utilized in the Rietveld method for the Fe_xO_y crystalline structures.

FeO (wustite)						
Face-centered cubic						Occupancy
FeO Fm3m (2 2 5)			Atomic fractional coordinates			
Atom	Type	Site	*x*	*y*	*z*	
Fe (1)	Fe^{2+}	4a	0.0000	0.0000	0.0000	0.02083
O (1)	O^{2-}	4b	0.5000	0.5000	0.5000	0.02083
FeO·Fe_2O_3 (magnetite)						
Cubic						Occupancy
FeO·Fe_2O_3 Fd3m (2 2 7)			Atomic fractional coordinates			
Atom	Type	Site	*x*	*y*	*z*	
O (1)	O^{2-}	32e	0.2577	0.2577	0.2577	0.16667
Fe (2)	Fe^{2+}	8a	0.1250	0.1250	0.1250	0.04167
Fe (1)	Fe^{3+}	16d	0.5000	0.5000	0.5000	0.08333
Fe_2O_3 (hematite)						
Rhombohedral						Occupancy
Fe_2O_3 R-3C (1 6 7)			Atomic fractional coordinates			
Atom	Type	Site	*x*	*y*	*z*	
Fe (1)	Fe^{3+}	6b	0.0000	0.0000	0.0000	0.1666
Fe (2)	Fe^{3+}	6a	0.0000	0.0000	0.2500	0.1666
O (1)	O^{2-}	18d	0.5000	0.0000	0.0000	0.5000

2. Experimental

2.1. Catalysts preparation

Fe_xO_y/C catalysts were prepared by the incipient wet impregnation method as follows: proper amounts of iron nitrate $Fe(NO_3)_3 \cdot 9H_2O$ (Sigma–Aldrich) were added to three different beakers each containing 10 ml of deionized water to obtain 15, 20 and 30 wt% of iron content on carbon. Afterwards, carbon (CARBOCHEM, with a surface area of 900 m^2/g) was added to the iron nitrate solutions under constant stirring for 5 min. Next, solids were filtered and dried at 373 K for 24 h, and then calcined in air at 773 K to obtain the final Fe_xO_y/C catalysts.

2.2. Characterization

2.2.1. X-ray diffraction and Rietveld refinement

X-ray diffraction data were obtained in a Bruker Advance D-8 diffractometer with a Cu Kα radiation source and a graphite secondary monochromator beam. Intensities were obtained in 2-theta ranges between 32° and 110° with a step of 0.01° and a measuring time of 10 s per point. The crystalline structures of iron oxides were refined by the Rietveld method using Rietica software [16] and the parameters shown in Tables 1 and 2 [17–19]. In order to find quantitative changes in the densities obtained by the Rietveld refinement, theoretical density (Table 2) for each phase was calculated by the following equation:

$$\rho = \frac{(Z)(MM)(\text{Avogadro's\_number})^{-1}}{\text{Cell\_volume}}$$

where *MM* is the atomic weight for each case and *Z* is the number of molecules/cell.

Table 2
Lattice parameters and angles utilized in the Rietveld method for the Fe_xO_y crystalline structures.

Lattice parameters			Angles			Density (g cm^{-3})
a	*b*	*c*	*α*	*β*	*γ*	
FeO (wustite)						
4.3070 Å	4.3070 Å	4.3070 Å	90°	90°	90°	5.973
FeO·Fe_2O_3 (magnetite)						
8.3811 Å	8.3811 Å	8.3811 Å	90°	90°	90°	5.223
Fe_2O_3 (hematite)						
5.0356 Å	5.0356 Å	13.7489 Å	90°	90°	120°	5.270

Theoretical atom occupancies were calculated using the Wyckoff multiplicities and the maximum multiplicity for each space group, as follows:

$$\text{Occupancy\_theoretical} = \frac{\text{Multiplicity}}{\text{Maximum\_multiplicity}}$$

The crystallite size (*D*) was estimated by the Scherrer equation, also included in Rietica software:

$$H_{LK} = \frac{180}{\pi}\frac{\lambda}{D}Sec(\theta) + \frac{180}{\pi}S * Tang(\theta)$$

where H_{LK} is the full-width at half-maximum (FWHM) of the contributing Lorentzian; *S* is the strain. λ is the wavelength of the radiation source used. θ is the diffraction peak position.

2.2.2. UV–vis absorption spectrum

UV–vis absorption spectra were obtained with a Varian Cary III UV–vis spectrophotometer coupled with an integration sphere for diffuse reflectance studies. A sample of MgO with 100% reflectance was used as reference.

2.2.3. Adsorption measurements

Nitrogen adsorption–desorption isotherms on Fe_xO_y/C substrates were obtained at 76 K with an automatic Quantachrome Autosorb 3B instrument. Prior to the adsorption run, all samples were outgassed overnight at 573 K. N_2 and He gases required for the operation of sorption apparatus were UHP-grade quality. The specific surface areas were calculated from the desorption isotherms using the BET equation whereas pore size distribution functions were obtained by non-local density functional theory for a slit pore model [20]. Considering the shortcomings inherent to the BJH analysis [21,22] for solids, as carbon with slit-type pores, the pore size distribution of these materials was determined by the NLDFT method [23,24] since it not only takes into account the variety of interaction potentials (i.e., solid–adsorbate, adsorbate–adsorbate, etc.) existing in the adsorption system, but also gives information about particularities in mechanistic aspects of the evaporation and condensation processes taking place inside cavities and throats [25]. The calculation of pore size distribution is based on a solution to the generalized adsorption isotherm equation, which correlates the kernel of theoretical adsorption/desorption isotherms with the experimental sorption isotherm:

$$N\left(\frac{P}{P^0}\right) = \int_{W_{MIN}}^{W_{MAX}} N\left(\frac{P}{P^0, W}\right) f(W)dW$$

where $N(P/P^0)$ is the experimental adsorption isotherm data, *W* is the pore width, $N(P/P^0,W)$ is the isotherm on a single pore of *W*, and *f*(*W*) is the pore size distribution function. The NLDFT permits the description of the adsorption process over a complete range of values, so it is possible to obtain a pore size distribution that extends over the complete micro-mesopore size range.

2.2.4. Fractal dimension

Fractal dimension is a quantitative (statistical) method used for comparing roughness patterns among solid surfaces. In this work, values of fractal dimension D_s were calculated from the adsorption–desorption isotherms data and the Frenkel-Halsey-Hill equation expressed as follows [26,27]:

$$Ln(S^{lg}) = const - (3 - D_s)Ln(\mu)$$

where S^{lg} is the amount adsorbed at the relative pressure P/P^0; *T* is the absolute temperature and μ is the so-called adsorption potential defined as:

$$\mu = RTLn\left(\frac{P^0}{P}\right)$$

2.2.5. Catalytic activity measurement

The catalytic photoactivity was evaluated using a 200 ml Pyrex batch reactor containing an aqueous ethanol-water solution (1:1 molar ratio) and 0.2 g of catalyst. Photo-irradiation was performed using a high pressure Hg lamp encapsulated in a quartz tube for a λ = 254 nm and intensity 4.4 mW. Circulation of gases was induced with a peristaltic pump. The reaction procedure was monitored by taking samples every hour then, subsequently analyzed with a gas chromatograph GC Varian 3800 having a TCD detector and a capillary column (Mol Sieve 5A), for their quantification.

3. Results and discussion

3.1. X-ray diffraction and Rietveld refinement

XRD patterns and Rietveld refinements for Fe_xO_y/C materials are shown in Fig. 1. Several peaks corresponding to the Bragg reflection planes of wustite (FeO), magnetite (FeO·F_2O_3) and hematite (Fe_2O_3) crystallites, are observed. The lattice parameters of iron oxides nanostructures were refined by the Rietveld method, and are reported in Tables 3a and 3b. Results for different iron contents showed that the most abundant crystalline phase was magnetite (more than 70 wt%) with crystallite sizes between 58 and 132 nm for samples of 15 and 20 wt% Fe content, respectively. The crystallite size for the two samples in the wustite phase was 14 and 3 nm, respectively. This result is due to an increase in the iron oxide content on the support sample increasing thus the liberation of oxygen from the surface of the wustite phase samples during the calcination process [28]. The liberation of oxygen increases the Fe^{2+} relative concentration and at the same time induces a gradient in the Fe^{2+} concentration on the wustite sample surface by diffusion through the crystalline phase network [28]. This diffusion phenomenon can be noticed by a decrease in the crystallite size of the wustite phase when the iron content increased from 15 to 20 wt% (Table 3a). It appears that there is a relationship between the Fe^{2+} occupancy number and the crystallite size. Changes in the occupancy values are point defects, and these can be Fe^{2+} deficiencies in the wustite network. Taking into account that FeO is metastable, a new phase as Fe_3O_4 can develop on its surface and increase its thickness by diffusion of Fe^{2+} ions through Fe_3O_4 [29]. On the other hand, when iron content on the support sample is increased up to 30 wt%, a new phase, named hematite, is formed (see Fig. 1). Fe_xO_y/C materials with 30 wt% Fe content have 21.97 wt% wustite; 75.17 wt% magnetite and 2.86 wt% hematite, respectively (Table 3a). This fact suggests that at a high iron content, the heat accumulated into the bulk of Fe_xO_y/C materials is maintained for a long time, causing the reorientation of some FeO and FeO·F_2O_3 to form Fe_2O_3 structures. This is possible because the thermodynamically metastable phases are wustite and

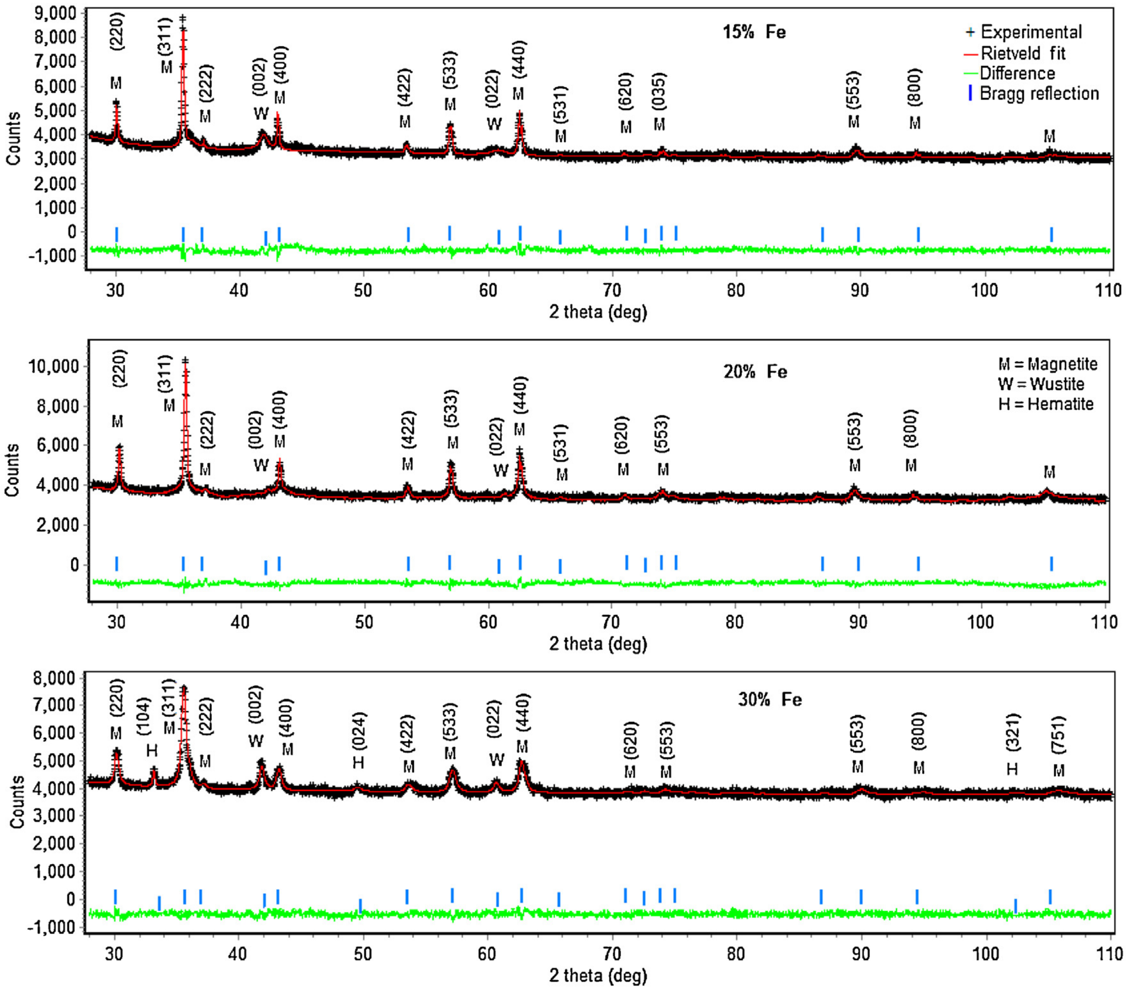

Fig. 1. Rietveld plot of Fe_xO_y/C catalysts. The upper curve marks correspond to experimental data and the continuous line, to those calculated; the lower curve is their difference. Thick marks correspond to M (magnetite), W (wustite) and H (hematite) accordingly, as indicated. Numbers in parenthesis correspond to different reflection planes (hkl) in the crystalline structures.

Table 3a
Rietveld refinement data for Fe_xO_y/C catalysts for different Fe content.

Phase	Weight (%)	Crystallite size (nm)	Occupancy		Density (g cm^{-3})
			[Fe^{3+}][(1)]	[Fe^{2+}][(2)]	
Fe_xO_y/C (15% Fe)					
Wustite	26.13	14 (1)	–	0.020 (1)	5.742
Magnetite	73.87	58 (2)	0.077 (1)	0.036 (1)	4.747
Fe_xO_y/C (20% Fe)					
Wustite	21.83	3 (1)	–	0.017 (1)	5.700
Magnetite	78.17	132 (12)	0.070 (1)	0.042 (1)	5.188
Phase	Weight (%)	Crystallite size (nm)	Occupancy		Density (g cm^{-3})
			[Fe^{3+}][(1, 2)]	[Fe^{2+}][(2)]	
Fe_xO_y/C (30% Fe)					
Wustite	21.97	17 (1)	–	0.021 (1)	5.970
Magnetite	75.17	35 (2)	0.067 (2)	0.038 (1)	4.630
Hematite	2.86	29 (4)	0.167 (1), 0.167 (1)	–	5.267

Wustite: FeO; magnetite: $FeO{\cdot}Fe_2O_3$; hematite: Fe_2O_3.
(1) and (2) parenthesis indicate different Fe atoms.

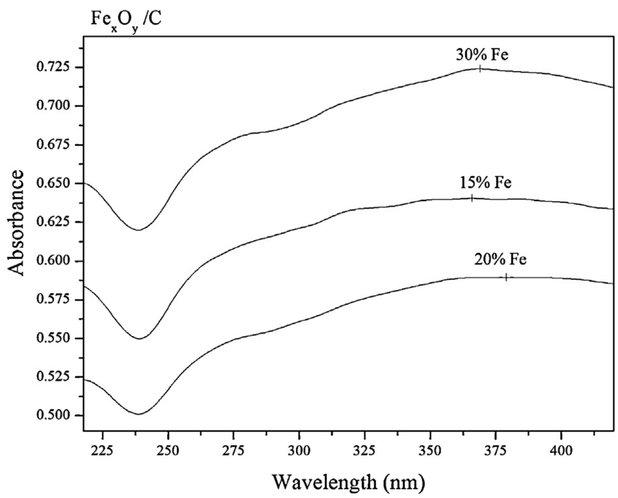

Fig. 2. UV–vis spectra for Fe_xO_y/C semiconductors at different Fe content.

magnetite [30]; meanwhile, hematite phase is thermodynamically stable [28,31].

3.2. UV–vis absorption spectra

UV–vis diffuse adsorption spectra of Fe_xO_y/C semiconductors at different iron content are shown in Fig. 2. A broad absorption band in the spectral region 325–425 nm has been assigned to the direct transition from 2p O^{2-} orbit electrons to the conduction band [32]. But iron oxides show three kinds of optical transitions: the ligand to metal charge-transfer transitions; the ligand field transitions (*d–d* transitions) and the pair excitations [33,34]. Fan et al. found, by TEM and UV–vis observations, some changes in the absorption bands of iron oxides that can be explained as a function of their geometric shapes [32]. Such shapes could be due to the iron oxide lattices with different atomic orientations, hence, differences between absorption bands of iron oxides could induce changes in the distribution of dipoles and electric fields. Although further investigation on the underlying mechanism of absorption band is necessary, the presence of different crystalline structures in Fe_xO_y/C semiconductors could explain differences between the absorption bands shown in Fig. 2. The differences lie in the structural properties of each one. By comparing Table 3a with Fig. 2, we can conclude the absorption capacity of solids depends of the Fe^{3+} content, as follows:

$$\text{absorptionat30 wt\%Fe} > \text{absorptionat15 wt\%Fe} > \text{absorptionat20 wt\%Fe}$$

Table 3b
Statistical parameters after the Rietveld refinement.

Sample	R_p	R_{wp}	χ^2	R_{exp}
At 15 wt% Fe_xO_y	1.7	2.2	1.6	1.7
At 20 wt% Fe_xO_y	2.0	2.6	2.5	1.6
At 30 wt% Fe_xO_y	1.4	1.8	1.4	1.5

R_p: profile *R*-factor.
R_{wp}: weighted profile *R*-factor.
χ^2: the goodness of fit.
R_{exp}: expected *R*-factor.

The absorbance of iron oxides has been attributed to the magnetic coupling and the excitation of Fe^{3+} neighbors, this enhances the *d–d* transitions, and leads to an increase in absorption [32], i.e., the greater concentration of Fe^{3+} cations in Fe_xO_y/C semiconductors implies a stronger absorption.

On the other hand, the concentrations of Fe^{3+} ions in Fe_xO_y/C semiconductors (Tables 1, 2 and 3a) follow the next order:

$$[Fe^{3+}]\text{at30 wt\%Fe} > [Fe^{3+}]\text{at15 wt\%Fe} > [Fe^{3+}]\text{at20 wt\%Fe}$$

These results show a good correlation between the absorbance spectra and the content of Fe^{3+} ions in Fe_xO_y/C semiconductors. This allows us to infer that magnetite and hematite phases play an important role in the photophysical properties of Fe_xO_y/C semiconductors.

3.3. Textural properties

The specific surface areas of Fe_xO_y/C substrates annealed at 773 K are reported in Table 4. Addition of iron oxide decreases notably the BET specific surface area of Fe_xO_y/C substrates when ranging from 638 to 490 m^2/g (as the iron content increases from 15 to 30 wt%). These results suggest that the intrawall pores and principal channels (these can be of micropores) are blocked by iron oxides deposits. The intrawall volume diminishes from 250 to 152 $mm^3\,g^{-1}$ and the micropore volume from 212 to 134 $mm^3\,g^{-1}$ as the iron content increases from 15 to 30 wt%.

On the other hand, the surface fractal dimension is another textural property which was estimated by statistical calculations from N_2 sorption data. This property allows us to tell the degree of roughness or tortuosity on Fe_xO_y/C surfaces. If roughness of surface is increased, fractal dimension will increase. So that both, the capture photons [35] and the diffusion processes of molecules toward Fe_xO_y/C surfaces, could be affected by the highly chaotic tortuosity when the dimension of the Euclidean surface is $D_s = 2$. However, if it happens to be $2 < D_s < 3$, the surface under study is occupying more space than any other surface but less space than a Euclidean volume. Therefore, $D_s \approx 3$, implies a too high degree of tortuosity.

The fractal analyses results of the N_2 sorption processes show the same value ($D_s = 2.9$) for all samples (Table 4 and Fig. 3a). This

Table 4
Pore structure parameters for Fe_xO_y/C catalysts.

Sample	S_{BET} (m^2/g)	S^{NLDFT} (m^2/g)	V_P^{NLDFT} ($mm^3\,g^{-1}$)	D_P^{NLDFT} (nm)	V_{iw}^{NLDFT} ($mm^3\,g^{-1}$)	V_{Mi} ($mm^3\,g^{-1}$)	D_s
15% Fe_xO_y/C	638	655	344 (37)	1.96 (0.16)	250	212	2.96
20% Fe_xO_y/C	448	451	242 (22)	1.96 (0.16)	176	164	2.96
30% Fe_xO_y/C	490	500	264 (39)	1.96 (0.20)/2.36 (0.08) 2.60 (0.17)	152	134	2.96

S_{BET} was calculated using the molecular cross-sectional area of N_2, 0.162 nm^2/molecule.
S^{NLDFT} was obtained by the NLDFT from the desorption branch.
V_P^{NLDFT}: total pore volume.
D_P^{NLDFT}: pore diameter taken from the maximum of the PSD curve. For samples with three-modal.
PSDs, three values are given.
V_{iw}^{NLDFT}: volume of intrawall.
V_{Mi}: micropore volume determinate by *t*-method.
D_s: surface fractal dimension.
The number in parenthesis corresponds to the standard deviation.

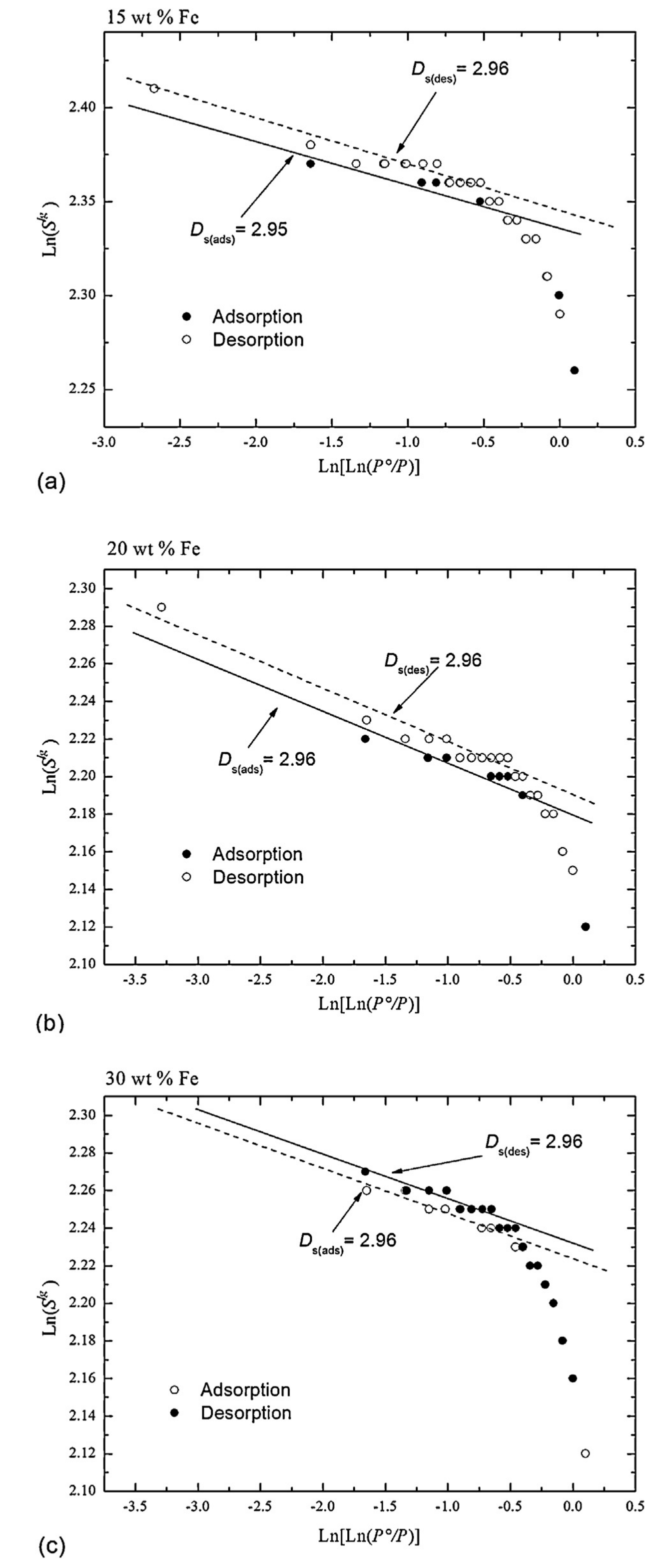

Fig. 3. Frenkel-Halsey-Hill fractal analysis of the adsorption–desorption isotherms of Fe_xO_y/C substrates at different Fe content.

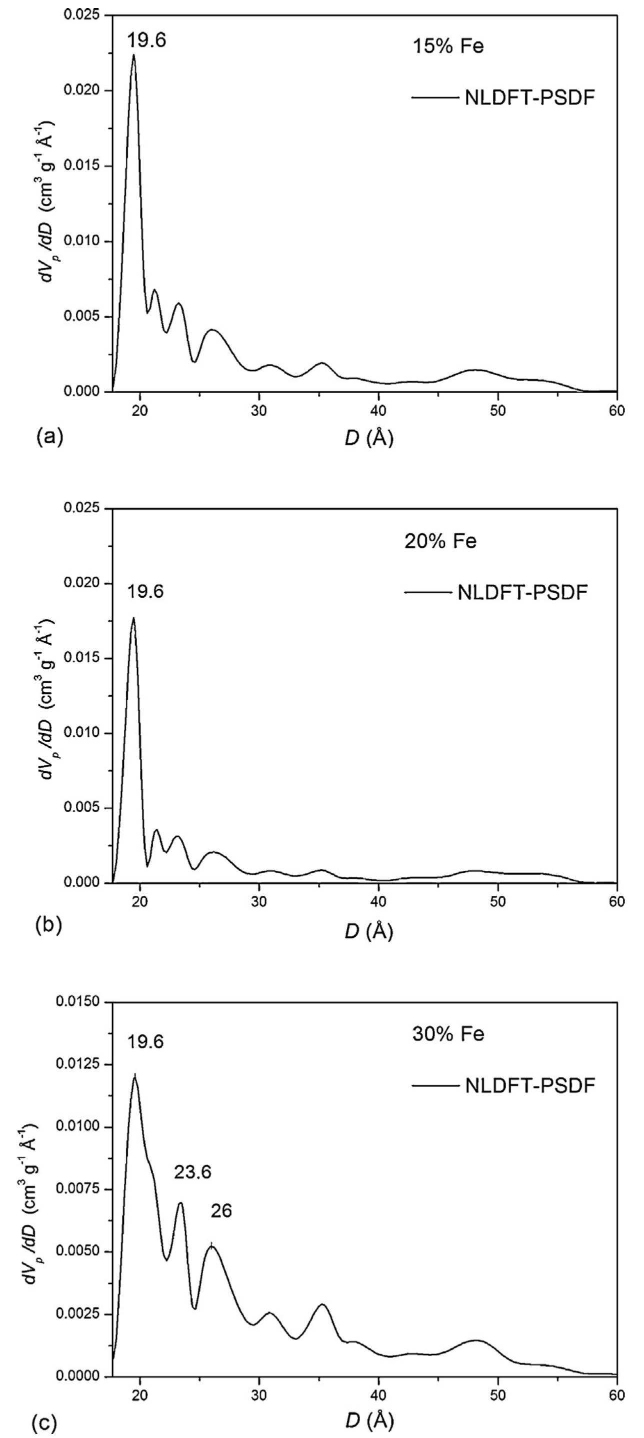

Fig. 4. Pore size distribution of Fe_xO_y/C substrates at different Fe content, calculated from the NLDFT model using desorption isotherms.

means: (i) Fe_xO_y loadings were not large enough to make differences on the topologies of surfaces under study, (ii) the high capacity of activated carbon to adsorb the iron nitrate solution is evident as a consequence of its high porosity built by slit-shaped pores.

Pore size distribution functions of Fe_xO_y/C substrates at 15, 20 and 30 wt% Fe content are shown in Fig. 4, so is their corresponding pore size diameter is reported in Table 4. At 15 and 20 wt% Fe, Fe_xO_y/C substrates portray similar monomodal pores system (1.96 nm of diameter); however at 30 wt% Fe, Fig. 4 shows a three-modal pore system (1.9, 2.3 and 26 nm of pore diameter). Fig. 5 shows loops of adsorption–desorption isotherms at 15, 20 and 30 wt% Fe content. Isotherms for substrates at 30 wt% Fe, present higher capacity for nitrogen adsorption than others containing 20 wt% Fe. This result indicates that modifications of the textural properties, due to changes in structural properties, take place. For

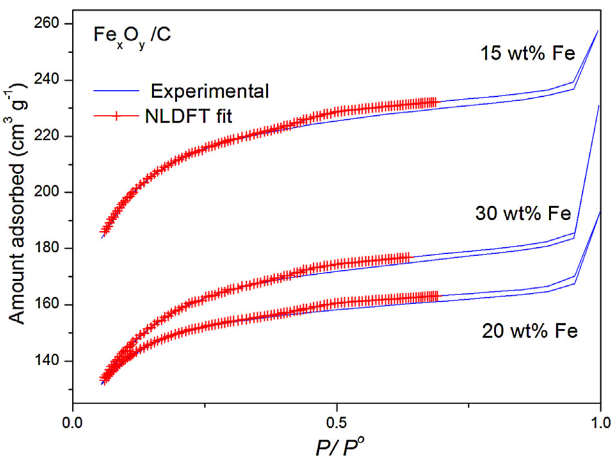

Fig. 5. Comparison of the experimental nitrogen desorption isotherm on Fe_xO_y/C substrates with the NLDFT isotherm in a slit pore at different Fe content.

example, new pores could appear due to the formation of hematite nanostructures.

This can be so because once iron nitrate solution was deposited on activated carbon, crystalline phases arose on their proper geometries. Yet, the shape of the crystalline phases growing within the pore walls played a role on final textural properties as is shown in Figs. 4 and 5. In particular, the hematite structure grows like a two-edged sword (see Figs. 5 and 6), a characteristic that allows it to break carbon materials internally [36].

3.4. Catalytic activity

The photocatalytic activities of Fe_xO_y/C photocatalysts were evaluated in hydrogen production from ethanol photodecomposition at room temperature. The amount of hydrogen produced was analyzed by gas chromatography. The hydrogen production evolution as a function of reaction time is plotted in Fig. 7. The apparent rate constant K was calculated by the Integral Method for an irreversible monomolecular zero order reaction [37]:

$$r_A = \frac{dC_A}{dt} = K$$

where C_A is the hydrogen concentration at time t, and K is the rate constant.

Fig. 8 displays an acceptable linearity obtained from data recorded in the first 6 h of reaction. The related data calculated from selected slopes are reported in Table 5. A maximum rate constant, $K = 2125\ \mu mol\ h^{-1}$, was obtained from the sample with 30 wt% Fe.

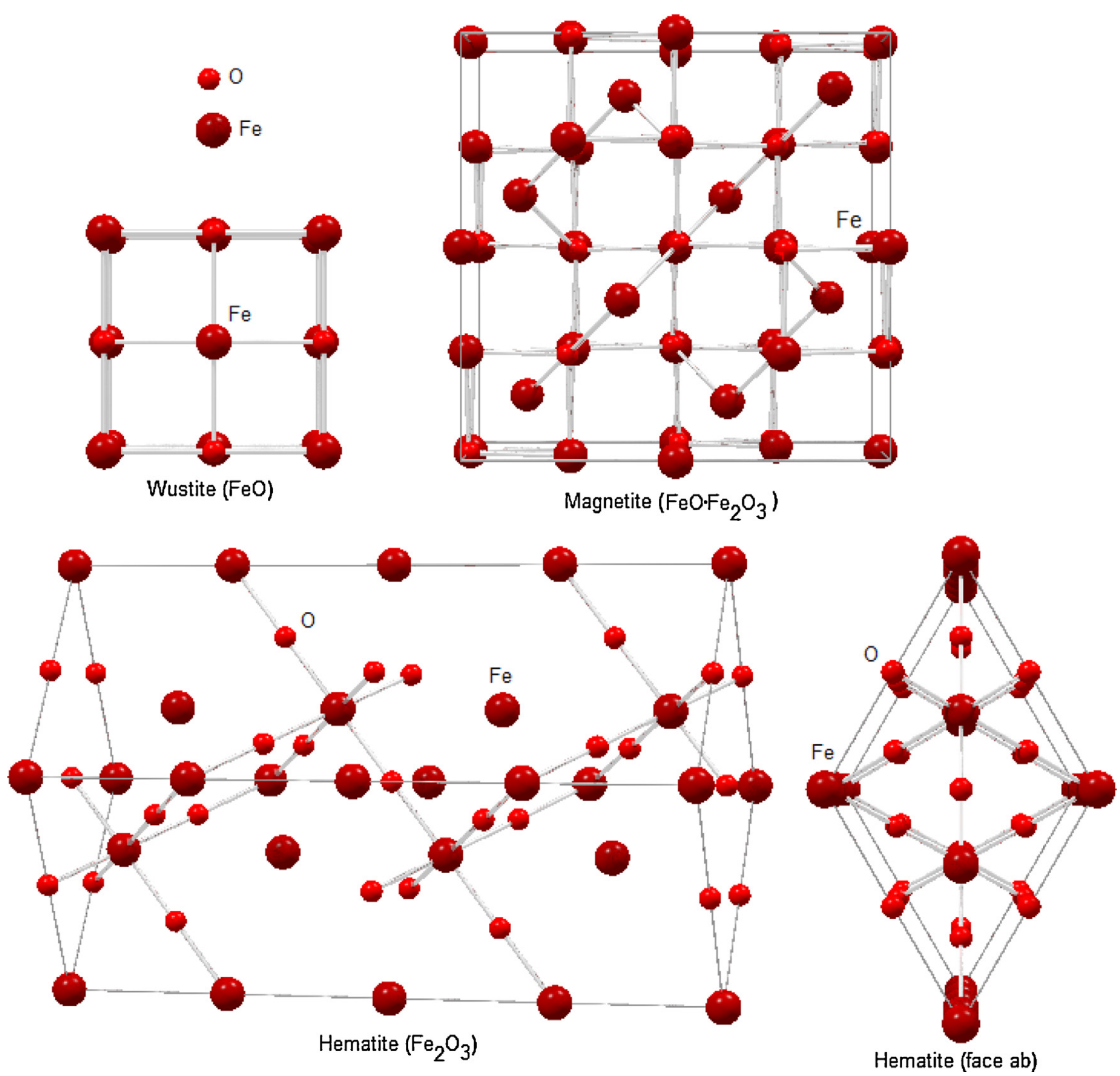

Fig. 6. Crystalline structures for iron oxides at the same scale.

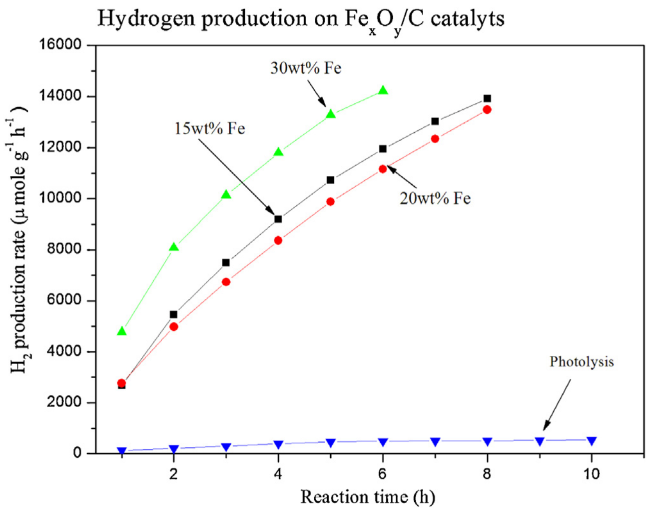

Fig. 7. Hydrogen production rate as a function of the reaction time.

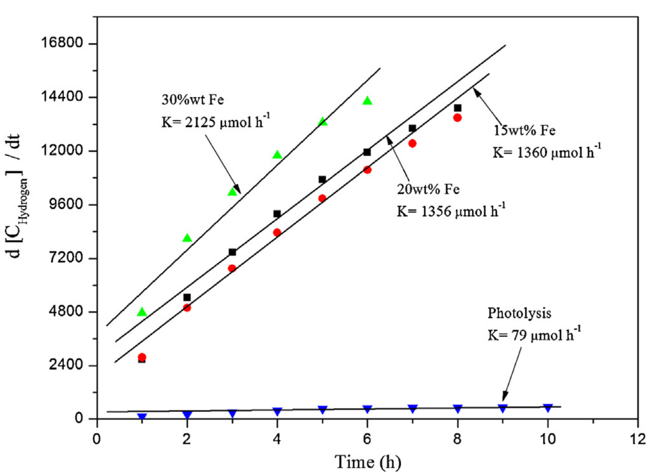

Fig. 8. Kinetic constant for the hydrogen production on Fe_xO_y/C photocatalysts.

Fig. 7 shows that the highest hydrogen production rate was achieved on catalysts at 30 wt% Fe. This exhibits the smallest crystallite size and the highest Fe^{3+} concentration in Fe_xO_y/C photocatalysts. Comparing the information portrayed in Figs. 7 and 8, a good correlation between the UV–vis absorbance and the catalytic activity is obtained. These satisfactory results allow us to propose that, for Fe_xO_y/C photocatalysts at 30 wt% Fe, the abundance of Fe^{3+} ions is the principal factor affecting the catalytic activity.

Xagas and coworkers found a correlation between fractality and ability to capture photons, that is, the semiconducting network is acting in a 'sponge'-like way [35]. Yet, this correlation is not satisfied in this work. Clearly, photoactivity is neither being dominated by fractality nor by any other textural properties as we can see by comparing Tables 4 and 5 with each other. Therefore, photoactivity should be subject to the photophysical properties of Fe_xO_y/C photocatalysts.

Table 5
Photoactivity for Fe_xO_y/C catalysts as a function of the Fe content.

Catalyst	Kinetic constant (μmol h^{-1})
Photolysis	79
Fe_xO_y/C at 15% Fe	1360
Fe_xO_y/C at 20% Fe	1356
Fe_xO_y/C at 30% Fe	2125

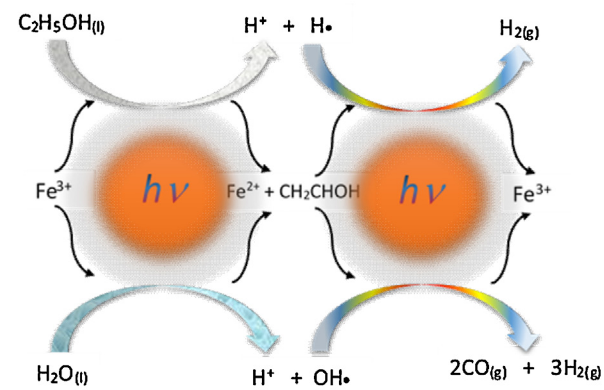

Fig. 9. Photoreactions mechanism involved on the hydrogen production on Fe^{3+} ions.

Those results may be due to the participation of the Fe^{2+}/Fe^{3+} redox cycle in reaction under the UV–vis radiation [38]. In this way, Fe^{3+} ions play an important role in the photodehydrogenation of ethanol; the following reaction mechanism is proposed:

$$Fe^{3+} + CH_3CH_2OH + h\nu \rightarrow Fe^{2+} + CH_2CHOH + H^+ + H\cdot \quad (3)$$

$$Fe^{2+} + H^+ + H\cdot \rightarrow Fe^{3+} + H_2 \quad (3')$$

$$Fe^{3+} + H_2O + h\nu \rightarrow Fe^{2+} + H^+ + \cdot OH \quad (4)$$

$$Fe^{2+} + H^+ + \cdot OH + CH_2CHOH \rightarrow Fe^{3+} + 2CO + 3H_2 \quad (4')$$

Finally, the overall reaction can be described as follows:

$$C_2H_5OH + H_2O \rightarrow 2CO + 4H_2$$

This mechanism starts by two undergoing simultaneous processes such as the photoreduction of Fe^{3+} and the catalytic photodehydrogenation of C_2H_5OH in aqueous solution, producing Fe^{2+} and CH_2CHOH. After this half cycle, another two simultaneous processes take place: water molecule was photocatalytically split into H^+ and $\cdot OH$ [39] and CH_2CHOH reacts with H^+ and $\cdot OH$ to transform into CO molecules and hydrogen. During this procedure Fe^{2+} was oxidized into Fe^{3+}. This novel mechanism is described in Fig. 9.

Note that the lixiviation processes for iron oxides demand intense conditions of pH and/or temperature [40]. In this work, the reactions were performed under mild conditions as already mentioned above, hence, we considered unnecessary quantify Fe_xO_y phases in Carbon after reaction.

4. Conclusions

Several roles of the iron content in the modifications of crystalline structure, textural properties and the photocatalytic activity of Fe_xO_y/C catalysts are reported in this paper. Increasing iron content alters not only the phase composition and crystallite size, but also surface area as well as intrawalls and micropores volumes. The capacity of UV–vis absorbance by Fe_xO_y/C catalysts significantly depends of the amount of Fe^{3+} ions present in the catalysts. There is a clear relationship between the UV–vis absorbance capacity; the Fe^{3+} concentration and the reaction rate constant for hydrogen production in the photodehydrogenation of ethanol. It can be concluded that variations in the structural properties of Fe_xO_y/C catalysts and the hydrogen production can be influenced by the Iron (III) concentration.

Acknowledgements

F. Galindo-Hernández thanks the financial support from CONACyT-51007 for his postdoctoral research. Authors are grateful to Dr. Manuel Aguilar for his technical assistance in the XRD analyses.

References

[1] G.P. Dinga, Hydrogen: the ultimate fuel and energy carrier, International Journal of Hydrogen Energy 14 (1989) 777.
[2] T.N. Veziroglu, Hydrogen energy system: next action, International Journal of Hydrogen Energy 11 (1986) 1.
[3] L.P. Bicelli, Hydrogen: a clean energy source, International Journal of Hydrogen Energy 11 (1986) 555.
[4] J.S. Jang, H.G. Kim, P.H. Borse, J.S. Lee, Simultaneous hydrogen production and decomposition of H_2S dissolved in alkaline water over CdS-TiO_2 composite photocatalysts under visible light irradiation, International Journal of Hydrogen Energy 32 (2007) 4786.
[5] N. Alenzi, W. Liao, P.S. Cremer, V. Sanchez-Torres, T.K. Wood, C. Ehlig-Economides, Z. Cheng, Photoelectrochemical hydrogen production from water/methanol decomposition using Ag/TiO_2 nanocomposite thin films, International Journal of Hydrogen Energy 35 (2010) 11768.
[6] P. Maruthamuthu, K. Gurunathan, E. Subramanian, M.V.C. Sastri, Visible light induced hydrogen production with Cu(II)/Bi_2O_3 and Pt/Bi_2O_3/RuO_2 from aqueous methyl viologen solution, International Journal of Hydrogen Energy 18 (1993) 9.
[7] K. Gurunathan, P. Maruthamuthu, M.V. Sastri, Photocatalytic hydrogen production by dye-sensitized Pt/SnO_2 and Pt/SnO_2/RuO_2 in aqueous methyl viologen solution, International Journal of Hydrogen Energy 22 (1997) 57.
[8] B. Naik, S. Martha, K.M. Parida, Facile fabrication of Bi_2O_3/$TiO_{2-x}N_x$ nanocomposites for excellent visible light driven photocatalytic hydrogen evolution, International Journal of Hydrogen Energy 36 (2011) 2794.
[9] V.V. Chesnokov, A.S. Chichkan, Production of hydrogen by methane catalytic decomposition over Ni–Cu–Fe/Al_2O_3 catalysts, International Journal of Hydrogen Energy 34 (2009) 2979.
[10] M. Frites, Y.A. Shaban, S.U.M Khan, Iron oxide (n-Fe_2O_3) nanowire films and carbon modified (CM)-n- Fe_2O_3 thin films for hydrogen production by photosplitting of water, International Journal of Hydrogen Energy 35 (2010) 4944.
[11] R. Dholam, N. Patel, M. Adami, A. Miotello, Hydrogen production by photocatalytic water-splitting using Cr- or Fe-doped TiO_2 composite thin films photocatalysts, International Journal of Hydrogen Energy 34 (2009) 5337.
[12] Y. Chen, K. Tu, Thickness dependent on photocatalytic activity of hematite thin films, International Journal of Photoenergy (2012), http://dx.doi.org/10.1155/2012/980595.
[13] A. Boudjemaa, S. Boumaza, M. Trari, R. Bouarab, A. Bouguelia, Physical and photo-electrochemical characterization of α-Fe_2O_3. Application for hydrogen production, International Journal of Hydrogen Energy 34 (2009) 4268.
[14] K. Weissermel, H. Arpe, Industrial Organic Chemistry, 1st ed., Reverte, Spain, 1981.
[15] M.F.R. Pereira, J.J.M. Órfão, J.L. Figueiredo, Oxidative dehydrogenation of ethylbenzene on activated carbon catalysts 3. Catalyst deactivation, Applied Catalysis A: General 218 (2001) 307.
[16] B.A. Hunter, C.J. Howard-Ansto, Rietica V2.1, Lucas Heights Laboratories, N.S.W, Australia, 2007.
[17] E.R. Jette, F. Foote, An X-ray study of the wüstite (FeO) solid solutions, Journal of Chemical Physics 1 (1933) 29.
[18] V.S. Coker, A.M.T. Bell, C.I. Pearce, R.A.D. Pattrick, G.V. Laan, J.R. Lloyd, Time-resolved synchrotron powder X-ray diffraction study of magnetite formation by the Fe(III)-reducing bacterium Geobacter sulfurreducens, American Mineralogist 93 (2008) 540.
[19] http://it.iucr.org/
[20] S. Lowell, J.E. Shields, M.A. Thomas, M. Thommes, Characterization of Porous Solids and Powders: Surface Area, Pore Size and Density, 1st ed., Kluwer Academic Publishers, Netherlands, 2004.
[21] M.L. Ojeda, J.M. Esparza, A. Campero, S. Cordero, I. Kornhauser, F. Rojas, On comparing BJH and NLDFT pore-size distributions determined from N2 on SBA-15 substrata, Physical Chemistry Chemical Physics 5 (2003) 1859.
[22] W.W. Lukens, P. Schmidt-Winkel, D. Zhao, J. Feng, G.D. Stucky, Evaluating pore sizes in mesoporous materials: a simplified standard adsorption method and simplified Broekhoff-De Boer method, Langmuir 15 (1999) 5403.
[23] P.I. Ravikovitch, A.V. Neimark, Density functional theory of adsorption in spherical cavities and pore size characterization of templated nanoporous silicas with cubic and three-dimensional hexagonal structures, Langmuir 18 (2002) 1550.
[24] A.V. Neimark, P.I. Ravikovitch, A. Vishnyakov, Bridging scales from molecular simulations to classical thermodynamics: density functional theory of capillary condensation in nanopores, Journal of Physics: Condensed Matter 15 (2003) 347.
[25] V. Mayagoitia, F. Rojas, I. Kornhauser, Pore network interactions in ascending processes relative to capillary condensation, Journal of the Chemical Society, Faraday Transactions 1 (1985) 2931.
[26] F. Wang, S. Li, Determination of the surface fractal dimension for porous media by capillary condensation, Industrial & Engineering Chemistry Research 36 (1997) 1598.
[27] A. Neimark, A new approach to the determination of the surface fractal dimension of porous solids, Physica A: Statistical Mechanics and its Applications 191 (1992) 258.
[28] http://www.siderurgia.org.ar/pdf/337.pdf
[29] F. Agullo-Lopez, C.R.A. Catlow, P.D. Townsend, Point Defects in Materials, 1st ed., Academic Press Inc., San Diego, 1988.
[30] J. Setién, J.A. Díez-Aja, Aproximación histórica y metalúrgica a los primeros hornos altos, Revista de Metalurgia 44 (2008) 299.
[31] J.D. Uribe, J. Osorio, O. Arnache, D. Giratá, A. Hoffmann, Revista Colombiana de Física 40 (2008) 1.
[32] H.M. Fan, G.J. You, Y. Li, Z. Zheng, H.R. Tan, Z.X. Shen, S.H. Tang, Y.P. Feng, Shape-controlled synthesis of single-crystalline Fe_2O_3 hollow nanocrystals and their tunable optical properties, Journal of Physical Chemistry C 113 (2009) 9928.
[33] Y.P. He, Y.M. Miao, C.R. Li, S.Q. Wang, L. Cao, S.S. Xie, G.Z. Yang, B.S. Zou, Size and structure effect on optical transitions of iron oxide nanocrystals, Physical Review B 71 (2005) 125411.
[34] M.D. Sherman, T.D. Waite, Electronic spectra of Fe^{3+} oxides and oxide hydroxides in the near IR to near UV, American Mineralogist 70 (1985) 1262.
[35] A.P. Xagas, E. Androulaki, A. Hiskia, P. Falaras, Preparation, fractal surface morphology and photocatalytic properties of TiO_2 films, Thin Solid Films 357 (1999) 173.
[36] X. Xu, M.B. Cortie, Precious metal core–shell spindles, Journal of Physical Chemistry C 111 (2007) 18135.
[37] O. Levenspiel, Chemical Reaction Engineering, 3rd ed., Wiley, New Delhi, India, 2007.
[38] C.A. Emilio, W.F. Jardim, M.I. Litter, H.D. Mansilla, EDTA destruction using the solar ferrioxalate advanced oxidation technology (AOT): comparison with solar photo-Fenton treatment, Journal of Photochemistry and Photobiology A: Chemistry 151 (2002) 121.
[39] J.E. McMurry, E.E. Simanek, Organic Chemistry, 6th ed., Cengage Learning, Inc., USA, 2007.
[40] Peter R. Tremaine, Jacques C. LeBlanc, The solubility of magnetite and the hydrolysis and oxidation of Fe^{2+} in water to 300 °C, Journal of Solution Chemistry 9 (1980) 415.